ACS Partner Journal

ARTIFICIAL PHOTOSYNTHESIS

Editors' Choice

Open Access



pubs.acs.org/artificialphotosynthesis

Article

# Oxygen-Mediated Sequential Down-Conversion in Perylenediimides

Yifan Bo, Nathalie Zink-Lorre, René Weiß, Ángela Sastre-Santos, Timothy Clark, Fernando Fernández-Lázaro,* and Dirk M. Guldi*

Cite This: https://doi.org/10.1021/aps.5c00002

Read Online



**ABSTRACT:** Perylenediimides (PDIs) are among the best-known chromophores for optoelectronic applications. Their photophysics in oxygen-rich environments remains, however, underexplored. In this study, we investigate three different PDI derivatives using steady-state and time-resolved absorption and emission spectroscopy in toluene with different oxygen concentrations. Unsubstituted PDI and 1,7-bay-substituted PDI featuring diphenylphenoxy groups exhibit oxygen-mediated sequential down-conversion. Upon photoexcitation, the singlet excited state ($S_1$) of PDIs interacts with molecular oxygen ($^3O_2$) to generate singlet oxygen ($^1O_2$) via the formation of the triplet excited state ($T_1$) of PDIs. Subsequently, ($T_1$)s of PDIs sensitize an additional $^3O_2$ to produce a second $^1O_2$. Overall, one ($S_1$) produces two $^1O_2$. Importantly, this process depends on energy requirements: on one hand, the energy difference between ($S_1$) and ($T_1$), and on the other hand, the ($T_1$) energy level should exceed that of $^1O_2$. Our work illustrates the oxygen-mediated sequential down-conversion in perylenediimides and reveals its effects.

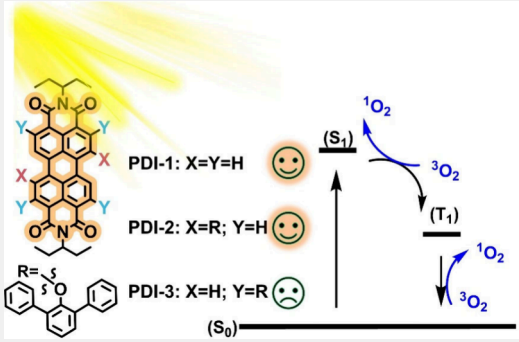


**KEYWORDS:** *singlet oxygen generation, down-conversion, perylenediimides, photophysics, triplet excited states*



## 1. INTRODUCTION

Perylenediimides (PDIs) and their derivatives are among the most extensively studied dyes due to their outstanding photophysical and chemical properties.[1,2] In particular, PDIs exhibit high molar absorption coefficients in the visible light region, high fluorescence quantum yields, and high thermal and chemical stability. All of the aforementioned renders them highly versatile for applications including optoelectronics, photovoltaics, and bioimaging.[3−10] Moreover, PDIs feature several positions, including bay-, *ortho*-, and imide-positions, which constitute a versatile platform for manipulating the overall chemical structure.[11,12]

Currently, the modification of PDIs has attracted considerable interest in the design of photocatalysts for water splitting, degradation of pollutants, to name just a few.[13−19] Among these, activating dioxygen ($O_2$) for the generation of reactive oxygen species (ROS) stands out due to its potential application in the fields of artificial photosynthesis[20,21] and photodynamic therapy.[22,23] However, the development of efficient PDI photocatalysts for ROS-driven photosynthesis is limited, especially when focusing on singlet oxygen generation.[14,19,24−26] ROS, such as hydrogen peroxide ($H_2O_2$), superoxide ($O_2^{\cdot-}$), and hydroxyl radicals ($^{\cdot}OH$) are produced by means of electron transfer process, whereas the generation of singlet oxygen ($^1O_2$) from ground-state triplet molecular oxygen ($^3O_2$) requires a mechanism to facilitate spin-state transitions, enabling the system to overcome spin-flip constraints inherent to the process.[27,28] By far the most common method to generate $^1O_2$ is energy transfer, that is, reacting a photosensitizer (PS) with $^3O_2$. This process starts with the photoexcitation of PS to create its singlet excited state ($S_1$), followed by intersystem crossing (ISC) ($S_1 \rightarrow T_1$) to populate the triplet excited state ($T_1$). Subsequently, $^1O_2$ is formed via a Dexter energy transfer from ($T_1$) of PS to $^3O_2$; ($T_1$) + $^3O_2 \rightarrow$ ($S_0$) + $^1O_2$.[29,30] Implicit is the fact that the $T_1$ energy of PS should be higher than the singlet−triplet energy gap of $O_2$ (0.976 eV). Notably, the ($T_1$)s of PDIs are reported to be around 1.15 eV, which meets the PS requirements.[31−33] For an efficient $^1O_2$ generation using PDI based PSs, nonradiative ISC must outcompete any radiative decays.

Despite recent reports on PDI derivatives that feature near-unity fluorescence quantum yields, significant singlet oxygen quantum yields ($\Phi_\Delta$), such as 36% for core-unsubstituted PDI[26] and 15% for tetra-pyridyl-substituted PDI,[14] were measured using 1,3-diphenylisobenzofuran (DPBF) as a singlet oxygen probe. Based on transient absorption spectroscopic measurements, PDI-pyrrolidine derivatives lack any long-lived ($T_1$) in oxygen-free solvents.[34,35] Some derivatives still reveal $\Phi_\Delta$s of roundabout 16%.[36] This puts a question mark over the reliability of singlet oxygen detection.[37] For example, DPBF as

**Received:** January 17, 2025
**Revised:** May 7, 2025
**Accepted:** May 7, 2025

a probe lacks specificity and reacts with superoxide species or even hydrogen peroxide.[38,39] A mechanistic understanding for affording such $\Phi_\Delta$s remains sketchy and vague. What is missing are photodynamic studies of PDIs that are performed under oxygenated conditions.

In this work, one core-unsubstituted PDI (**PDI-1**)[40] and two core-substituted PDIs with diphenylphenoxy groups at the 1,7-bay (**PDI-2**)[41] and 2,5,8,11-*ortho* positions (**PDI-3**),[42] for which near unity $\Phi_F$s have been reported, were synthesized and investigated (Figure 1).[41,43,44] Oxygen effects on the

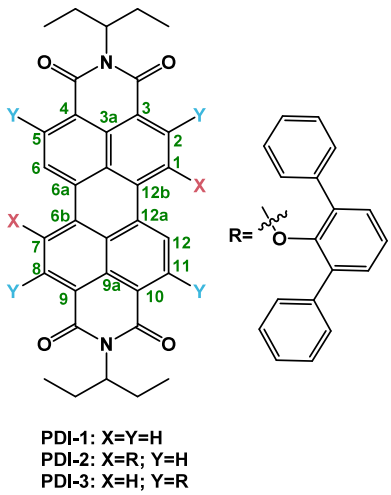


**Figure 1.** Chemical structures of **PDI-1**, **PDI-2**, and **PDI-3**.

photophysical dynamics, including $^1O_2$ generation, of these PDIs were probed by steady-state and time-resolved spectroscopies. Density-functional theory (DFT) and time-dependent DFT (TD-DFT) calculations provided independent confirmation of the experimental results. To avoid aggregation, concentrations of less than $10^{-5}$ M were used. In oxygen-free toluene, none of the PDIs exhibit any detectable ISC or $(T_1)$ formation. In, however, the presence of oxygen, **PDI-1** and **PDI-2** exhibited a sequential down-conversion, in which one $(S_1)$ produces two $^1O_2$ with $^3O_2$ and $(T_1)$ as intermediate. Notably, the oxygen-mediated sequential down-conversion contributed to 37% of $\Phi_\Delta$ for **PDI-2** in $O_2$-saturated toluene, as well as 30% of $\Phi_\Delta$ for **PDI-1**. Overall, the energy levels of $(S_1)$ and $(T_1)$ are proven essential with the requirements of $E(S_1) - E(T_1) > 0.976$ eV and $E(T_1) > 0.976$ eV. This sequential down-conversion mechanism is potentially applicable to all PDIs possessing appropriate $(S_1)$ and $(T_1)$ energy levels. These findings not only enrich our knowledge of the photophysical properties of PDIs but also provide deeper insights into oxygen-mediated sequential down-conversion, paving the way for broader applications of PDIs in photosensitization and singlet oxygen generation technologies.

## 2. OVERVIEW OF THE OXYGEN-MEDIATED SEQUENTIAL DOWN-CONVERSION

In oxygen-mediated sequential down-conversion, two steps are considered (Figure 2). In the initial step, the chromophore is photoexcited to its $(S_1)$. Subsequently, $(S_1)$ transitions to $(T_1)$ in a spin-allowed singlet−triplet annihilation involving the excited chromophore and $^3O_2$: $(S_1) + {}^3O_2 \rightarrow (T_1) + {}^1O_2$. This reaction is well-established and requires a singlet−triplet energy gap of the PS to exceed the energy of $^1O_2$ and, in

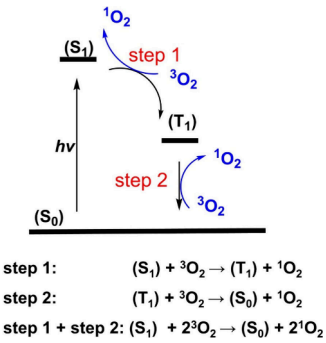


**Figure 2.** Kinetic scheme of oxygen-mediated sequential down-conversion.

turn, to satisfy the condition: $E(S_1) - E(T_1) > 0.976$ eV.[28] For PDIs, this reaction occurs in the diffusion-control limit.[27,28] In the second step, a second $^1O_2$ is sensitized by $(T_1)$, which is generated in the first step: $(T_1) + {}^3O_2 \rightarrow (S_0) + {}^1O_2$. This step also proceeds under diffusion-controlled conditions if the $(T_1)$ energy is higher than that of $^1O_2$ ($E(T_1) > 0.976$ eV). In summary, oxygen mediates a sequential down-conversion as shown in Figure 2. In this process, $(S_1)$ of the chromophore is subject to a two-step energy transfer, resulting in two $^1O_2$ after absorbing a single photon. $(T_1)$ of the chromophore serves hereby as an intermediate. Such an oxygen-mediated, sequential down-conversion potentially increases the efficiency of $^1O_2$ generation.

## 3. EXPERIMENTAL SECTION

Steady-state UV−vis absorption spectroscopy was carried out with a UV-1900i (Shimadzu) two-beam spectrophotometer. Steady-state fluorescence spectroscopy was recorded using an Edinburgh FS5 spectrometer. Time-correlated single photon counting (TCSPC) experiments were carried out with a Spectrofluorometer FS5 system from Edinburgh Instruments, integrated with an operating software called Fluoracle. A pulsed UV−vis picosecond laser system from PicoQuant was used to generate the excitation pulses. The fluorescence decay curve fits and lifetime analyses were performed with the software Fluoracle from Edinburgh Instruments. A Horiba Jobin Yvon FluoroLog3 emission spectrometer with a Symphony II detector in the near-infrared (NIR) detection range recorded the singlet oxygen emission spectra. The analysis and quantification of singlet oxygen quantum yield ($\Phi_\Delta$) was done using the relative method.[45] In this study, $C_{60}$ in toluene was used as a reference ($\Phi_{\Delta,\,C60} = 0.98$).[46] All spectra were acquired at room temperature using 10 × 10 mm quartz glass cuvettes. Oxygen/Argon purging was conducted by continuously flowing high-purity oxygen/Argon gas for 15 min under gentle flow conditions, as indicated by the steady formation of bubbles in the sealed cuvette. The cuvette was equipped with both gas inlet and outlet needles to maintain a constant atmosphere and minimize solvent evaporation.

Cyclic voltammetry (CV) and differential pulse voltammetry (DPV) were performed in distilled dichloromethane solutions (purged with Ar for 15 min) containing 0.1 M tetrabutylammonium hexafluorophosphate ($TBAPF_6$) as supporting electrolyte. Potentials were applied by a $\mu$Autolab III/FRA2 potentiostat (METROHM) controlled by the PC. The measurements were conducted in a home-built three-electrode configuration system. A glassy platinum (2 mm diameter), a platinum wire and a silver wire were employed as the working,


https://doi.org/10.1021/aps.5c00002
Artif. Photosynth. XXXX, XXX, XXX−XXX

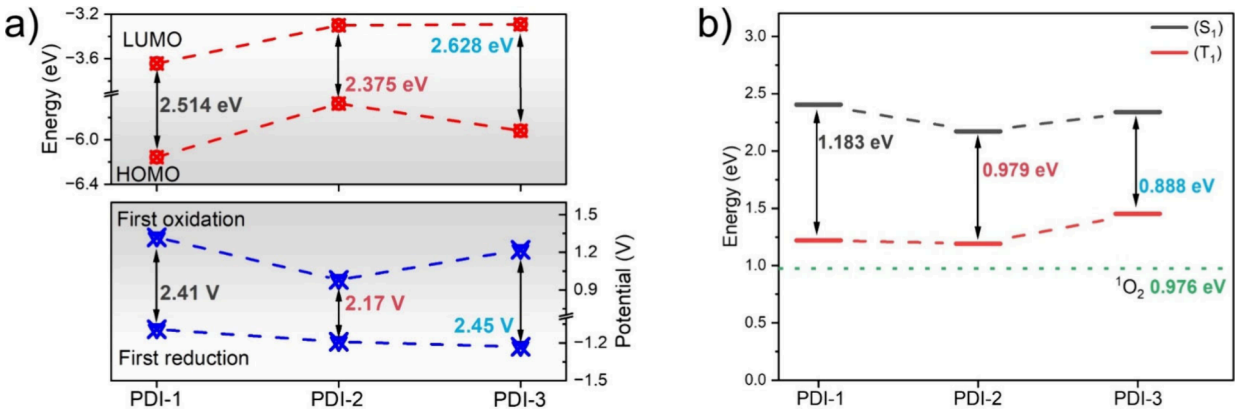


**Figure 3.** (a) Summary of the calculated HOMO/LUMO energies (top) and the first oxidations/reductions based on differential pulse voltammetry measurement shown in Figure 4a (bottom) of **PDI-1**, **PDI-2**, and **PDI-3**. (b) Energy-level diagram illustrating the calculated vertical transitions of $(S_1)$ and $(T_1)$ as well as vertical $(S_1) - (T_1)$ energy gaps for **PDI-1**, **PDI-2**, and **PDI-3** in comparison to $^1O_2$.

**Table 1. Steady-State Absorption Maxima $\lambda_{abs}$, Fluorescence Maxima $\lambda_{em}$, Fluorescence Quantum Yields $\Phi_F$, and Singlet Oxygen Quantum Yields $\Phi_\Delta$ of PDI-1, PDI-2, and PDI-3 in Toluene**

| | $\lambda_{abs}$ (nm) | $\lambda_{em}$ (nm) | $E(S_1)$[a] (eV) | $\Phi_F$[b] | $\Phi_\Delta$[c] |
|---|---|---|---|---|---|
| PDI-1 | 458/489/525 | 535/577/626 | 2.340 | 100%[d]/95%[e]/78%[f] | 9%[e]/30%[f] |
| PDI-2 | 481/516/555 | 575/617/679 | 2.206 | 94%[d]/88%[e]/73%[f] | 12%[e]/37%[f] |
| PDI-3 | 465/498/537 | 547/591/645 | 2.292 | 80%[e] | - |

[a]$E(S_1)$ is determined by the cross-pointing of normalized absorption and emission spectra. [b]This value is determined by a relative method using **PDI-1** in toluene after Ar-purging 15 min ($\Phi_F$ = 100%) as a standard. [c]This value is determined by a relative method using $C_{60}$ in toluene ($\Phi_\Delta$ = 98%) as a standard. [d]Samples are measured after 15 min Ar-purging. [e]Samples are measured in ambient conditions. [f]Samples are measured after 15 min $O_2$-purging.

counter, and reference electrode, respectively. Ferrocene (Fc) was used as an internal standard and all the potentials were given relative to the $Fc/Fc^+$ couple. The scan rate was kept at 50 mV/s for CV.

Ultrafast pump−probe transient absorption spectroscopy (TAS) was performed using an Astrella-F-1K amplified Ti:sapphire femtosecond laser system from Coherent, operating at a repetition rate 1 kHz, 5.5 W power (5 mJ pulse energy), pulse duration of 80 fs. To acquire the time-resolved transient absorption spectra on a subps or ns resolution, an Ultrafast Systems HELIOS or EOS fs/ns transient absorption spectrometer was used with time delays from 0 to 7000 ps and 1 ns to 400 $\mu$s, respectively. For subps, white light for the probing pulse in the visible region of the optical spectrum was generated by focusing part of the fundamental 800 nm output onto a 2 mm sapphire disk. For ns time scale experiments, white light for probing was generated by a photonic crystal fiber supercontiuum laser with a 1064 nm fundamental. The excitation wavelength was generated via a TOPAS Prime from Light Conversion with standard NirUVis extension. Data evaluation of fs-TAS and ns-TAS was conducted by a combination of multiwavelength and global analysis using the GloTarAn software, which is a free, Java-based graphical user interface to the R-package TIMP.[47−49]

The molecular structure was initially conformationally optimized using the global optimizer algorithm (GOAT, ORCA 6.0, GFN2-xTB).[50,51] The global minimum structure was further optimized with density-functional theory (DFT) at the B3LYP-GD3BJ/def2svp level in Gaussian16.[52−55] Excited states were calculated using time-dependent density functional theory (TD-DFT) at the same level as for the geometry optimizations. Excited states were calculated in the gas phase. The Avogadro software was used as a visualization for the computation result.[56]

## 4. RESULTS AND DISCUSSION

**4.1. Density-Functional Theory Calculations.** First, the molecular structures of PDIs were conformationally optimized using the global optimizer algorithm (GOAT, ORCA 6.0, GFN2-xTB).[50,51] These structures of the global minima were further optimized with density-functional theory (DFT) at the B3LYP-GD3BJ/def2svp level in Gaussian16.[52−55] Afterward, the frontier molecular orbital (FMO) analysis and the excited-state energy levels of **PDI-1**, **PDI-2**, and **PDI-3** were calculated.

The molecular-orbital surfaces of the highest occupied molecular orbitals (HOMOs) and lowest unoccupied molecular orbitals (LUMOs) and their relative energy levels for **PDI 1−3** are shown in Figures 3a and S1−S3. For **PDI-1**, both HOMO and LUMO are localized on the perylene core with energy levels of −6.156 and −3.642 eV, respectively. The corresponding HOMO − LUMO gap, ($\Delta E_g$) is 2.514 eV. Attaching electron-donating diphenylphenoxy groups at either the bay (**PDI-2**) or *ortho* (**PDI-3**) positions increases the frontier-orbital energy levels of **PDI-2** and **PDI-3**. Notably, the LUMOs of **PDI-2** and **PDI-3** are delocalized on the perylene core and the oxygen heteroatom sites with LUMO energies of −3.300 and −3.291 eV, respectively. In **PDI-2**, with diphenylphenoxys in the bay region, the HOMO is delocalized across the PDI core, oxygen atoms, and slightly onto the diphenylphenoxy groups. Therefore, the energy increase of the HOMO to −5.675 eV is larger than that of the LUMO to −3.300 eV. As such, **PDI-2** displays the lowest $\Delta E_g$ of 2.375 eV among the three PDIs. In contrast, the HOMO of **PDI-3** is localized on the PDI core and on the oxygen atoms. Its energy


https://doi.org/10.1021/aps.5c00002
Artif. Photosynth. XXXX, XXX, XXX−XXX

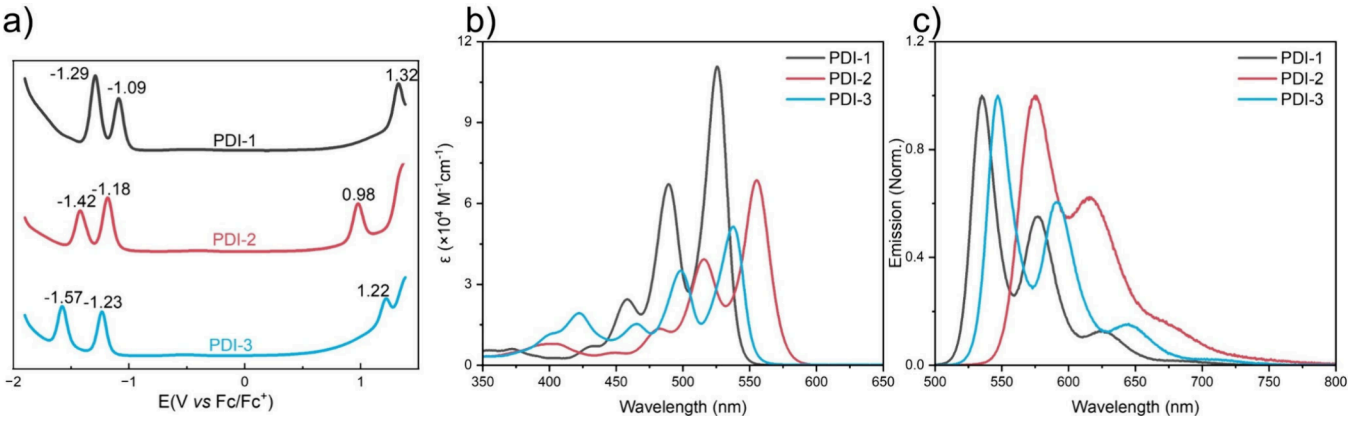


**Figure 4.** (a) Differential pulse voltammetry in degassed dichloromethane with 0.1 M $TBAPF_6$ as supporting electrolyte. A Pt (2 mm diameter) glass, a platinum wire, and a silver wire were employed as working, counter, and reference electrodes, respectively. Ferrocene (Fc) was used as an internal standard and all the potentials are given relative to $Fc/Fc^+$. (b) Steady-state absorption and (c) normalized steady-state fluorescence spectra in toluene at ambient conditions of **PDI-1**, **PDI-2**, and **PDI-3**.

level of −5.919 eV lies between that of **PDI-1** and **PDI-2**. $\Delta E_g$ of **PDI-3** is larger than that of **PDI-1** with 2.628 eV. Notably, the calculated results are consistent with the electrochemical properties observed in differential pulse voltammetry measurements (Figure 3a, *vide infra*), indicating that the electronic structures of **PDI-2** and **PDI-3** are modulated by attaching diphenylphenoxy groups.

The vertical excitation of ($S_1$) and ($T_1$) of PDI derivatives were calculated by time-dependent DFT (TD-DFT) at the B3LYP-GD3BJ/def2svp level; their excitation energy, assignments, and oscillator strength ($f$) are shown in Table S1. The calculated vertical energies of ($S_1$) are 2.404, 2.171, and 2.339 eV for **PDI-1**, **PDI-2**, and **PDI-3**, respectively, which match with the absorptions (*vide infra*, Table 1). For **PDI-1** and **PDI-2**, ($S_1$) is found to be HOMO→LUMO, with high $f$-values of 0.735 and 0.409, respectively (Figures S1−S2 and Table S1). As discussed in the FMO analysis, the HOMO→LUMO transition in **PDI-2** is locally excited (LE) with slight charge-transfer (CT) character. In **PDI-3**, however, ($S_1$) contains 61.6% HOMO→LUMO and 36.2% HOMO−1→LUMO and an oscillator strength as low as 0.171. Here, HOMO−1 is mainly localized on one of the diphenylphenoxy groups (Figure S3). To describe ($S_1$) of **PDI-3** better, the natural transition orbitals (NTOs) are shown in Figure S4. The HO-NTO is localized on the perylene core, oxygen heteroatom site, and one of the diphenylphenoxy groups, but the LU-NTO lacks contributions of the latter. In short, ($S_1$) of **PDI-3** exhibits mostly LE-character with a minor CT-contribution. For ($T_1$), the vertical energies of **PDI-1**, **PDI-2**, and **PDI-3** are 1.221, 1.192, and 1.451 eV, respectively (Table S1). Moreover, for all PDIs, ($T_1$)s are dominated by HOMO→LUMO. All three ($T_1$)s exceed the energy of $^1O_2$ with 0.976 eV and, in turn, enable step 2 of Figure 2. The vertical energy gaps between ($S_1$) and ($T_1$) ($E(S_1) - E(T_1)$) are 1.183, 0.979, and 0.888 eV for **PDI-1**, **PDI-2**, and **PDI-3**, respectively. Importantly, the $E(S_1) - E(T_1)$ of **PDI-1** is 0.207 eV greater than the energy of $^1O_2$. For **PDI-2**, the vertical energy gap is only 0.03 eV larger than the energy needed to activate $^1O_2$. The vertical energy gap is, however, 0.135 eV below the energy of $^1O_2$ in **PDI-3**. **PDI-3** falls short of the energy requirements for step 1 of the oxygen-mediated, sequential down-conversion. **PDI-1** and **PDI-2** satisfy the energy requirement.

**4.2. Steady-State Characterization.** The electrochemical properties were studied by cyclic voltammetry (CV) and differential pulse voltammetry (DPV) in degassed dichloromethane (Figures 3a and 4a; Figure S5). **PDI-2** and **PDI-3** feature distinct reductions and oxidations compared to **PDI-1** with their electron donating diphenylphenoxy groups. The presence of the latter renders the reduction of **PDI-2** and **PDI-3** harder at −1.19 V and −1.23 V, respectively, relative to that of **PDI-1** at −1.09 V. Oxidation of **PDI-2** and **PDI-3**, on the other hand, is facilitated. In particular, **PDI-2** displays the lowest oxidation at +0.98 V followed by **PDI-3** at +1.22 and 1.32 V for **PDI-1**. As shown in Figure 3a, the experimental DPV trends correlate well with the theoretical results.

In toluene, steady-state absorption and fluorescence spectra of **PDI-1**, **PDI-2**, and **PDI-3** exhibit the characteristic vibronic fine-structure of PDIs under ambient conditions, as shown in Figures 4b and 4c and summarized in Table 1. The absorption of **PDI-1** maximizes at 525 nm, with a molar extinction coefficient ($\varepsilon$) of ca. $1.11 \times 10^5$ $M^{-1}cm^{-1}$. Its fluorescence is a mirror image with a 535 nm maximum. **PDI-2** and **PDI-3** exhibit red-shifted and broadened absorption and fluorescence. For **PDI-2**, the absorption is red-shifted to 555 nm and $\varepsilon$ is $0.69 \times 10^5$ $M^{-1}cm^{-1}$. Its fluorescence is even further red-shifted to 575 nm. For **PDI-3**, the corresponding absorption and fluorescence maxima are found at 537 and 547 nm, respectively. And **PDI-3** displayed the lowest $\varepsilon$ with $0.51 \times 10^5$ $M^{-1}cm^{-1}$. The decrease of $\varepsilon$ (**PDI-1:** $1.11 \times 10^5$ > **PDI-2**: $0.69 \times 10^5$ > **PDI-3**: $0.51 \times 10^5$ $M^{-1}cm^{-1}$) correlates well with the trend seen for the TD-DFT calculated $f$ (**PDI-1:** 0.735 > **PDI-2**: 0.409 > **PDI-3**: 0.171). Decreasing $\varepsilon$ and $f$ imply an intensity reduction of the $\pi$-$\pi^*$ transitions across the series, which is attributed to differences in their electronic structures (*vide supra*).[57,58]

The effects of $O_2$ on the steady-state optical properties of the PDIs investigated were explored by measuring their steady-state absorption, fluorescence, and singlet-oxygen emission under three different conditions: Ar-purging (no $O_2$), ambient atmosphere (low $O_2$), and $O_2$-purging (high $O_2$) (Figure 5 and Table 1). First, the photophysics of the three PDIs in Ar-purging toluene were investigated to uncover the intrinsic photophysical properties. Taking **PDI-1** in toluene after Ar-purging ($\Phi_F$ = 100%) as a reference, **PDI-2** exhibits a lower $\Phi_F$ with 94%, and **PDI-3** displays the lowest $\Phi_F$ with 80% in the


https://doi.org/10.1021/aps.5c00002
Artif. Photosynth. XXXX, XXX, XXX−XXX

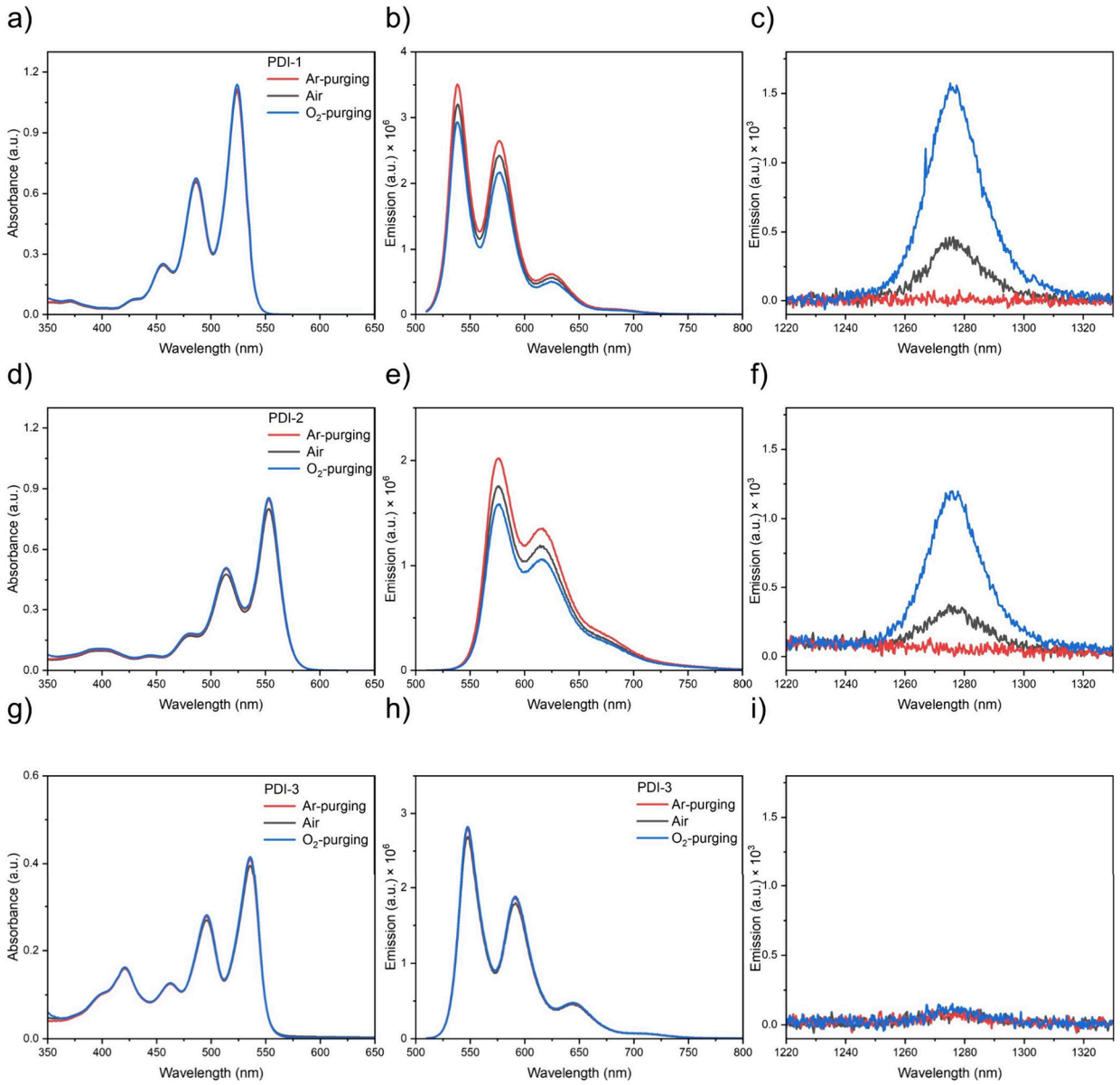


**Figure 5.** (a, d, g) Steady-state absorption, (b, e, h) fluorescence, and (c, f, i) singlet oxygen emission of (top, a–c) **PDI-1**, (middle, d–f) **PDI-2**, and (bottom, g–i) **PDI-3** under three different environmental conditions: Ar-purging (red), ambient atmosphere (black), and $O_2$-purging (blue).

same environment. To gain deeper insights, the radiative ($k_r$) and nonradiative ($k_{nr}$) rate constants of the three PDIs were determined (Full details are shown in the Supporting Information). As a cross check, we note that decreased $k_r$s (**PDI-1:** $2.08 \times 10^8$ > **PDI-2**: $1.59 \times 10^8$ > **PDI-3**: $1.38 \times 10^8$ $s^{-1}$) align well with the decreases in $\varepsilon$ and $f$.[58−60] In contrast, $k_{nr}$s give rise to an opposite trend (**PDI-1:** 0 < **PDI-2**: $0.10 \times 10^8$ > **PDI-3**: $0.34\times 10^8$ $s^{-1}$). In the absence of intersystem crossing (ISC) (*vide infra*), enhanced nonradiative decays in **PDI-2** and **PDI-3** are attributed to the conformational flexibility stemming from the diphenylphenoxy substituents, which enable intramolecular motions and, in turn, facilitate nonradiative transitions.[61,62]

Next, the three PDIs were compared under different $O_2$ concentrations. **PDI-1** and **PDI-2** exhibit similar behaviors. Their fluorescence starts to decrease as the $O_2$ concentration increases, while the singlet oxygen emission increases. We conclude that ($S_1$)s of **PDI-1** and **PDI-2** are quenched by $O_2$ to generate $^1O_2$. For example, fluorescence quantum yields ($\Phi_F$) of **PDI-1** decrease from 100% upon Ar-purging to 95% in ambient air and to 78% upon $O_2$-purging. The singlet oxygen quantum yield ($\Phi_\Delta$) of **PDI-1** increases from 9% under ambient conditions to 30% after $O_2$ purging, using $C_{60}$ in toluene as a standard ($\Phi_\Delta$ = 98%). For **PDI-2** which has a lower thermodynamic driving force for ($S_1$) + $^3O_2$→ ($T_1$) + $^1O_2$, $\Phi_F$ values are 94%, 88%, and 73% in toluene upon Ar-purging, ambient atmosphere, and $O_2$-purging conditions, respectively. Correspondingly, $\Phi_\Delta$s are 12% in an ambient atmosphere and increase to 37% after $O_2$-purging. No differences were observed in **PDI-3** under any conditions: No $^1O_2$ emission is observed for **PDI-3** regardless of the solvent. We hypothesize that no process of ($S_1$) + $^3O_2$ → ($T_1$) + $^1O_2$ plays a role in **PDI-3**.

**4.3. Time-Resolved Characterization.** For **PDI-1** and **PDI-2**, the quenching of ($S_1$) is further confirmed by time-correlated single-photon counting (TCSPC) (Figure S6 and


https://doi.org/10.1021/aps.5c00002
Artif. Photosynth. XXXX, XXX, XXX−XXX

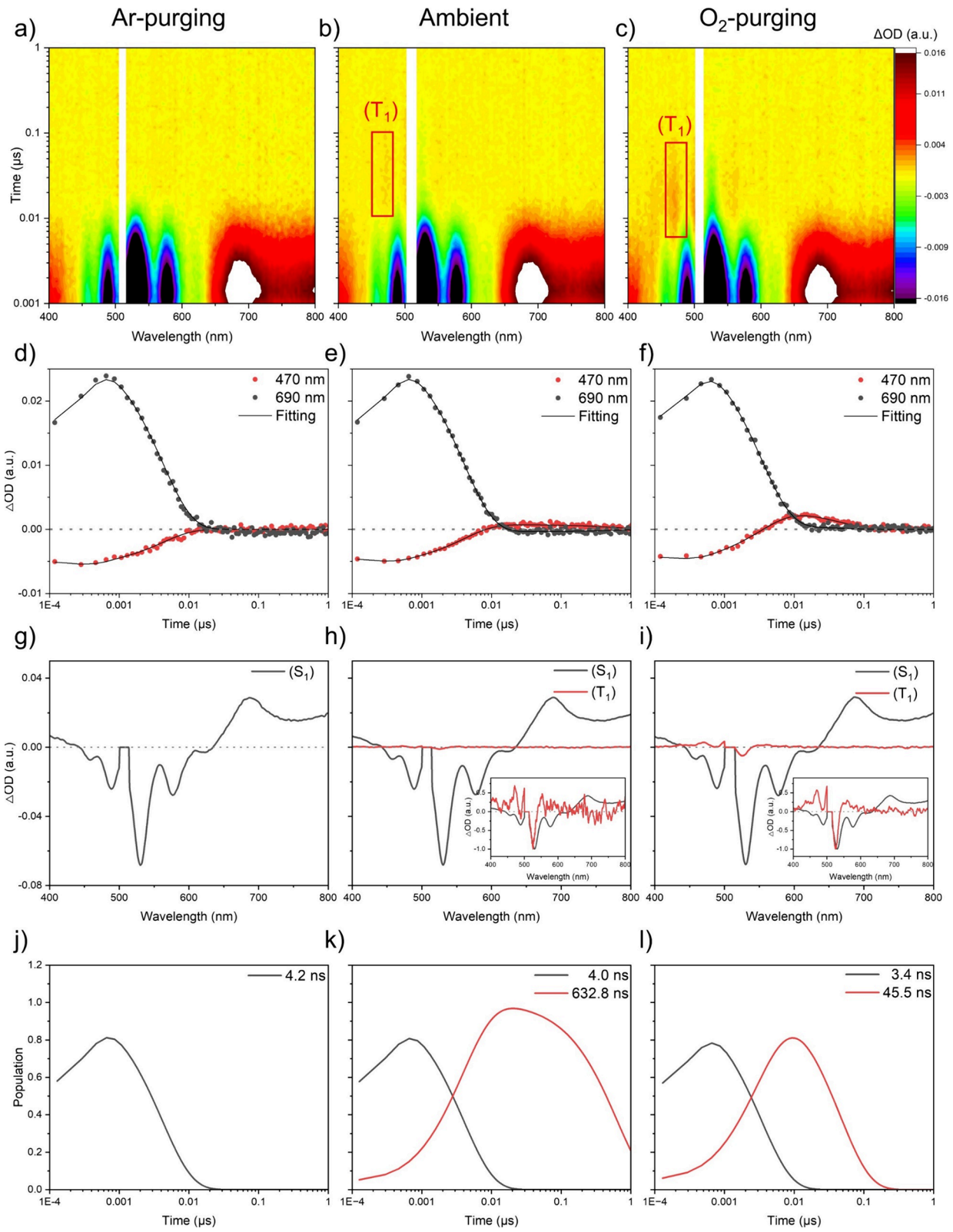


**Figure 6.** Nanosecond transient absorption spectroscopy (ns-TAS) of **PDI-1** in toluene at (left) Ar-purging, (middle) ambient atmosphere, and (right) $O_2$-purging conditions. (a−c) Heat-map of ns-TAS raw data obtained from pump−probe experiments at 510 nm photoexcitation. (d−f) Time absorption profiles as well as corresponding fits of selected wavelengths (see the figure legend for details). (g−i) Evolution-associated spectra (EAS) showing the relaxed singlet excited state ($S_1$) (black) and the triplet excited state ($T_1$) (red). Inset: normalized EAS. (j−l) Relative populations of the respective states.

Table S2). In toluene and under Ar, the fluorescence follows a monoexponential decay with a lifetime of 4.8 ns. Under ambient conditions and after $O_2$-purging, the fluorescence of **PDI-1** in toluene is still monoexponential, but the lifetimes are


https://doi.org/10.1021/aps.5c00002
Artif. Photosynth. XXXX, XXX, XXX−XXX

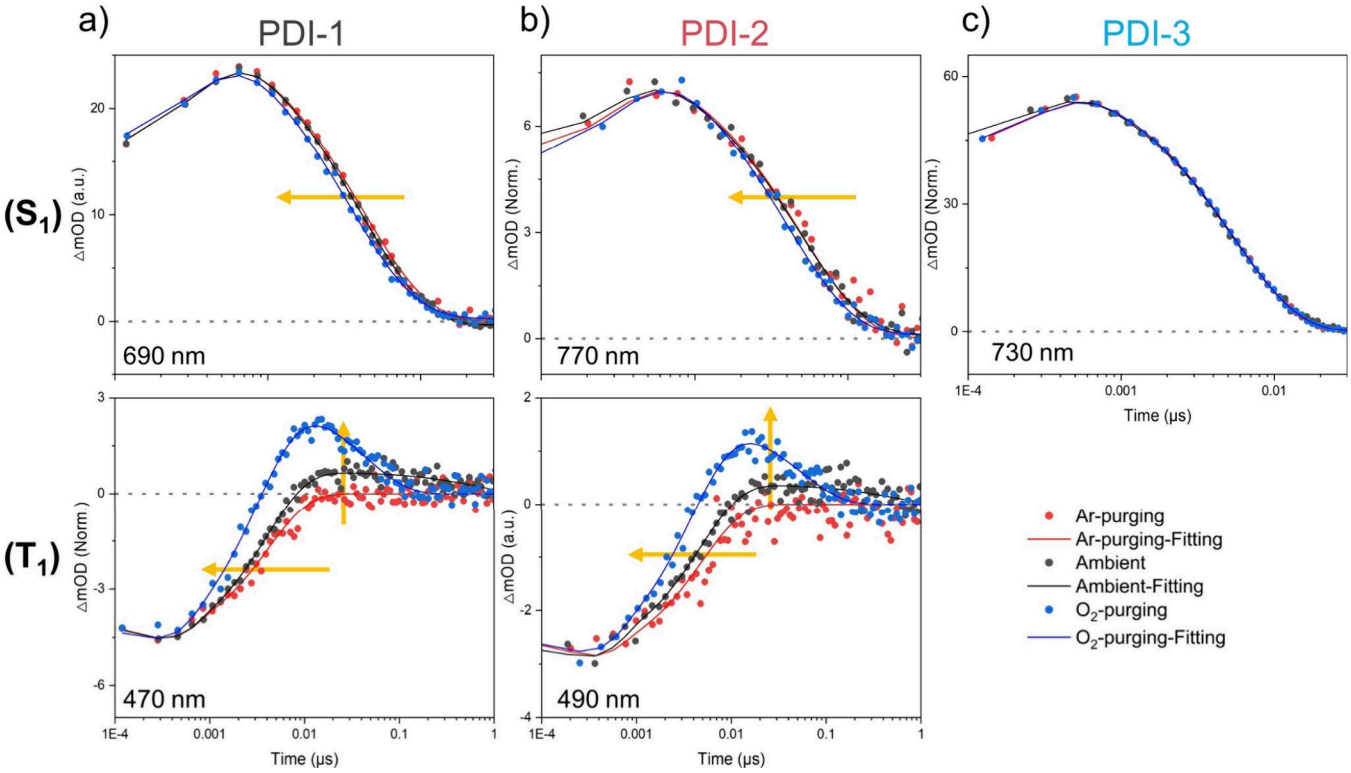


**Figure 7.** Time absorption profiles obtained from ns-TAS as well as corresponding fits of selected wavelengths of (top) the triplet excited state ($T_1$) signatures and (bottom) the singlet excited state ($S_1$) signatures of (a) **PDI-1**, (b) **PDI-2**, and (c) **PDI-3** in toluene under three different conditions: Ar-saturated (red), ambient atmosphere (black), and $O_2$-saturated (blue).

4.5 and 4.0 ns, respectively. A similar trend evolves for **PDI-2**, where ($S_1$) is quenched by $O_2$ and leads to shorter and shorter fluorescence lifetimes as the $O_2$ concentration is increased. Hereby, **PDI-2** features slightly longer lifetimes than **PDI-1** under identical conditions; 5.9 ns after Ar purging, 5.4 ns in ambient air, and 4.6 ns after $O_2$ purging. **PDI-3** behaves distinctly differently with a 5.8 ns lifetime regardless of the conditions. This indicates that ($S_1$) of **PDI-3** is not susceptible to $O_2$-quenching, in sound agreement with the results obtained from the steady-state assays.

Next, femto- and nanosecond transient absorption (fs- and ns-TAS) were performed to further investigate the excited state dynamics of the three PDIs. As TCSPC results suggest, oxygen is unlikely to exert any appreciable impact on the excited state dynamics in the femtosecond time range. For fs-TAS measurements, we focused on toluene as solvent after Ar-purging. As shown in Figures S7a−S9a, the vibrationally hot singlet excited state $(S_1)_{hot}$ of the PDIs in toluene are generated with the conclusion of photoexcitation. Raw data from fs-TAS experiments of the three PDIs were best fitted by global analysis with a sequential kinetic model based on two species via Glotaran.[63] (Figures S7−S9; Table S3). Both of these species exhibit identical spectroscopic features. On this basis, we assign them as the vibrationally hot singlet excited state $(S_1)_{hot}$ and the relaxed singlet excited state ($S_1$), that is, prior and after relaxation to the minimum of the potential energy surface via structural relaxation and solvent reorganization. The lifetime of $(S_1)_{hot}$ varied for the different PDIs: 2.9, 10.4, and 42.8 ps for **PDI-1**, **PDI-2** and **PDI-3**, respectively. We rationalize this observation by the structural flexibility and the diphenylphenoxy substitution that slow down structural relaxation. It is noted that ($S_1$) of the three PDIs is not completely deconvoluted on fs-TAS time scale.

ns-TAS was performed to explore the fate of ($S_1$) and the effects of $O_2$ on the excited-state dynamics. A sequential global analysis of the raw data was carried out via Glotaran.[63] The raw data and fitting results are shown in Figures 6, 7, S10, and S11 and Table S3. For **PDI-1** in toluene after Ar-purging, ns-TAS exhibits the same spectroscopic features as observed in fs-TAS, namely, the overlap of ground state bleaching (GSB) and stimulated emission (SE) in the range from 400 to 650 nm with minima at 457, 489, 530, 570, and 623 nm along with two excited-state absorptions (ESAs) in the range from 400 to 442 and from 650 to 800 nm (Figure 6a and d). The aforementioned characteristics remain across the range of excited-state dynamics. The raw data is best fitted by a singlet-species sequential mode, yielding a lifetime of 4.2 ns, which matches that observed in TCSPC. Therefore, it is the same as the second species in fs-TAS analyses, namely the relaxed singlet excited state ($S_1$) (Figures 6g and 6j).

For **PDI-1** in toluene under ambient conditions, the initial characteristics of ns-TAS are the same as ($S_1$) observed when purged with Ar (Figures 6b and 6e). Interestingly, new ESAs in the 400−500 and 550−650 nm ranges with maxima at 470 and 560 nm are discernible at a delay of ca. 10 ns. ns-TAS data of **PDI-1** in toluene under ambient conditions are best fitted by a sequential mode based on two species (Figures 6h and 6k). The first species exhibits spectral features identical to those of ($S_1$) observed in the **PDI-1** when $O_2$ is absent. Therefore, we attribute it to ($S_1$). Notably, the ($S_1$) lifetime of **PDI-1** under ambient conditions is shorter at 4.0 ns. The second species displays two ESAs in the range of 400−500 and 550−650 nm with ESA maxima at 470 and 560 nm, respectively, next to a


https://doi.org/10.1021/aps.5c00002
Artif. Photosynth. XXXX, XXX, XXX−XXX

GSB minimum of 525 nm, in excellent agreement with the ($T_1$) characteristics found in previous investigations.[64,65] The ($T_1$) lifetime is 632.8 ns. Consequently, when $O_2$ is present, ($T_1$) formation sets in for **PDI-1** via ($S_1$) + $^3O_2$ → ($T_1$) + $^1O_2$. Moreover, ($T_1$) of **PDI-1** is shorter-lived under ambient conditions than the microseconds typically reported.[35,66] Implicit is a ($T_1$) quenching by $O_2$ via ($T_1$) + $^3O_2$ →($S_0$) + $^1O_2$. The oxygen-mediated, sequential down-conversion of **PDI-1** is further confirmed through ns-TAS in toluene after $O_2$-purging (Figures 6c,f,i,l and 7a). At first glance, no differences were noted. In particular, ($S_1$) transitions to ($T_1$) by the mediation of $^1O_2$ (Figures 6c and 6f). Subtle differences emerged, however, when comparing the kinetics of ($S_1$) and ($T_1$) (Figure 7a). In fact, the ($S_1$) ESA at 690 nm tends to become shorter-lived as more $O_2$ is present and the ($T_1$) ESA formation at 470 nm becomes faster. But, also the ($T_1$) ESA at 470 nm is shorter-lived. To quantify these differences, ns-TAS of **PDI-1** at $O_2$-saturation is best fit using a kinetic model with two sequential species, ($S_1$) and ($T_1$) (Figures 6i and 6l). It is noted that the quenching of ($S_1$), ($S_1$) + $^3O_2$ → ($T_1$) + $^1O_2$, and ($T_1$), ($T_1$) + $^3O_2$ → ($S_0$) + $^1O_2$, are both diffusion-controlled and affected by the concentration of $O_2$. ($S_1$) and ($T_1$) lifetimes are 3.4 and 45.5 ns with $O_2$ and 4.0 and 632.8 ns under ambient conditions, which prompts to an oxygen-mediated sequential down-conversion in **PDI-1**.

All ns-TAS raw data and fitting results of **PDI-2** in toluene are shown in Figure 7b, Table S3, and Figure S10. The effects of $O_2$ on the excited-state dynamics of **PDI-2** are similar to those observed for **PDI-1**. In toluene, after Ar-purging to remove $O_2$, **PDI-2** is photoexcited to afford ($S_1$) with its 4.9 ns decay lifetime to ($S_0$) without showing any evidence of ($T_1$) involvement. In the low $O_2$ concentration range, that is, under ambient conditions, we note for **PDI-2** ($S_1$) and subsequently ($T_1$), with lifetimes of 4.8 and 484.5 ns, respectively. Both are shorter in the high $O_2$ concentration range with values of 4.0 and 55.4 ns, respectively. In summary, **PDI-2** is subject to an oxygen-mediated sequential down-conversion.

Finally, the effects of $O_2$ on the excited-state dynamics of **PDI-3** were investigated (Figures 7c and S11; Table S3). Regardless of the presence or absence of oxygen, **PDI-3** is photoexcited to ($S_1$) and subsequently decays back to the singlet ground state ($S_0$) with ca. 5.4 ns in ns-TAS measurements. No ($T_1$) formation is observed. This trend agrees well with the observations made in TCSPC experiments, that the fluorescence lifetime is unaffected by $O_2$. Therefore, **PDI-3** fails to undergo an oxygen-mediated sequential down-conversion.

**4.4. Stability.** The ultimate goal is to exploit efficient $O_2$ sensitizers of high chemical stability. The PDI derivatives in toluene solution were stored in individual clean sealed vials under well-lit ambient conditions and steady-state absorption spectra recorded periodically over 20 days. Under these conditions, all PDI derivatives exhibit excellent ambient stability (Figures S9 and S10). The high chemical stability of **PDI-1** and **PDI-2** emphasizes their robust ground and excited states despite oxygen-mediated sequential down-conversion occurring readily.

**4.5. Discussion.** Our study demonstrates the oxygen-mediated sequential down-conversion in **PDI-1** and **PDI-2**, which not only sheds light on the influence of oxygen on the excited-state dynamics but also offers a new strategy for designing efficient $^1O_2$ sensitizers. Based on our theoretical and experimental results, the essential criteria for energy level matching in oxygen-mediated sequential down-conversion has been established. For **PDI-1** and **PDI-2**, where the energy gap between ($S_1$) and ($T_1$) is larger than 0.976 eV, which is the energy of $^1O_2$, efficient ($S_1$) quenching and enhanced ($T_1$) formation are observed as the concentration of $O_2$ increases. An energy gap lower than 0.976 eV in **PDI-3** renders the ($S_1$) dynamics unaffected by $O_2$. In short, the energy gap between ($S_1$) and ($T_1$) is decisive in ensuring the thermodynamic feasibility of the first step, that is, ($S_1$) + $^3O_2$ → ($T_1$) + $^1O_2$. Moreover, ($T_1$) energies higher than 0.976 eV in **PDI-1** and **PDI-2** trigger an efficient quenching of ($T_1$). Recently, Buckup and co-workers demonstrated that $^3O_2$ catalyzes SF in pentacenes.[67] For TIPS-Pn, which fulfills $E(S_1) - E(T_1) >$ 0.976 eV, ($S_1$) of TIPS-pentacene (TIPS-Pn) sensitizes $^3O_2$. In turn, $^1O_2$ and ($T_1$) much like seen for **PDI-1** and **PDI-2** is generated in the first step. In the second step, $^1O_2$ interacts, however, with another TIPS-Pn in its ($S_0$) and produces a second ($T_1$) to complete SF rather than generating a second $^1O_2$ via ($T_1$) quenching. An $E(T_1) <$ 0.976 eV permits the earlier pathway in the case of pentacene, but an $E(T_1) >$ 0.976 eV for **PDI-1** and **PDI-2** renders it possible. In the case of pentacene, $^1O_2$ is consumed in the second step via ($S_0$) + $^1O_2$ → ($T_1$) + $^3O_2$. The effects of $O_2$ on the photophysics of TIPS-tetracene (TIPS-Tn) and its photodegradation have been described by Huang et al.[68] A ($T_1$) energy level of TIPS-Tn of >0.976 eV, which is similar to that of **PDI-1** and **PDI-2**, should prevent ($T_1$) sensitization by $^1O_2$. Instead, a second $^1O_2$ is sensitized by ($T_1$) of TIPS-Tn generated in the first step: ($T_1$) + $^3O_2$ → ($S_0$) + $^1O_2$. Consequently, $^1O_2$ formation in TIPS-Tn proceeds via the same sequential down-conversion as we observed for **PDI-1** and **PDI-2**. A similar reactivity has been reported for anthracene by fulfilling $E(S_1) - E(T_1) >$ 0.976 eV and $E(T_1) >$ 0.976 eV.[69] Importantly, $^1O_2$ decomposes acenes. This susceptibility poses a significant challenge to the practical applications and investigations of (poly)acenes in $^1O_2$ photosensitization. In a nutshell, experiments, calculations, as well as previous investigations, support the fact that $O_2$ mediates the sequential down-conversion in **PDI-1** and **PDI-2**. As such, we formulate the requirements for the oxygen-mediated sequential down-conversion as $E(S_1) - E(T_1) >$ 0.976 eV and $E(T_1) >$ 0.976 eV. Notably, we report for the first time on the $O_2$-mediated sequential down-conversion of PDI derivatives.

## 5. CONCLUSIONS

In this study, we investigated the oxygen effects on the photophysics of PDI derivatives comprehensively. By comparing different PDI derivatives, we have demonstrated oxygen-mediated sequential down-conversion to produce $^1O_2$ in **PDI-1** and **PDI-2**. This process is based on a two-step mechanism: ($S_1$) + $^3O_2$ → ($T_1$) + $^1O_2$ and ($T_1$) + $^3O_2$ → ($S_0$) + $^1O_2$. Overall, the energy requirements are confirmed to be a singlet−triplet energy gap, on one hand, and triplet energy, on the other hand, that both must exceed the relative energy of $^1O_2$. Notably, singlet oxygen quantum yields of 37% were observed for **PDI-2** upon $O_2$-saturation in toluene. The results of our study are important for a deeper understanding of the photophysics of PDIs and their derivatives and for a new strategy to design singlet oxygen sensitizers.


https://doi.org/10.1021/aps.5c00002
Artif. Photosynth. XXXX, XXX, XXX−XXX

## ■ ASSOCIATED CONTENT

### Supporting Information

The Supporting Information is available free of charge at https://pubs.acs.org/doi/10.1021/aps.5c00002.

Absorbance, emission, transient absorption spectroscopy, cyclic voltammetry, and photostability tests (PDF)

## ■ AUTHOR INFORMATION


### Corresponding Authors

**Fernando Fernández-Lázaro** − *Área de Química Orgánica, Instituto de Bioingeniería, Universidad Miguel Hernández de Elche, 03203 Elche, Spain;* orcid.org/0000-0002-4598-6024; Email: fdofdez@umh.es

**Dirk M. Guldi** − *Department of Chemistry and Pharmacy & Interdisciplinary Center for Molecular Materials (ICMM), FAU Profile Center Solar, Friedrich-Alexander-Universität Erlangen-Nürnberg, 91058 Erlangen, Germany;* orcid.org/0000-0002-3960-1765; Email: dirk.guldi@fau.de

### Authors

**Yifan Bo** − *Department of Chemistry and Pharmacy & Interdisciplinary Center for Molecular Materials (ICMM), FAU Profile Center Solar, Friedrich-Alexander-Universität Erlangen-Nürnberg, 91058 Erlangen, Germany;* orcid.org/0000-0002-4531-4789

**Nathalie Zink-Lorre** − *Área de Química Orgánica, Instituto de Bioingeniería, Universidad Miguel Hernández de Elche, 03203 Elche, Spain;* orcid.org/0000-0003-3081-995X

**René Weiß** − *Department of Chemistry and Pharmacy & Interdisciplinary Center for Molecular Materials (ICMM), FAU Profile Center Solar, Friedrich-Alexander-Universität Erlangen-Nürnberg, 91058 Erlangen, Germany;* orcid.org/0000-0002-7278-8111

**Ángela Sastre-Santos** − *Área de Química Orgánica, Instituto de Bioingeniería, Universidad Miguel Hernández de Elche, 03203 Elche, Spain;* orcid.org/0000-0002-8835-2486

**Timothy Clark** − *Department of Chemistry and Pharmacy & Computer-Chemie-Center (CCC), Friedrich-Alexander-Universität Erlangen-Nürnberg, 91052 Erlangen, Germany;* orcid.org/0000-0001-7931-4659

Complete contact information is available at: https://pubs.acs.org/10.1021/aps.5c00002


### Author Contributions

The manuscript was written through contributions of all authors. All authors have given approval to the final version of the manuscript.

### Notes

The authors declare no competing financial interest.

## ■ ACKNOWLEDGMENTS

D.M.G. acknowledges financial support from the Deutsche Forschungsgemeinschaft (DFG) GU 517/32-1. F.F.-L. thanks Grant PID2022-140315NB-I00 funded by MICIU/AEI/10.13039/501100011033 and by ERDF/EU. A.S.-S. and F.F.-L. are also indebted to the Generalitat Valenciana (CIPROM/2021/059) and the Advanced Materials program by MCIN with funding from European Union NextGenerationEU (PRTR-C17.I1) and Generalitat Valenciana (MFA/2022/028). Y.B. acknowledges a fellowship from the Chinese Scholarship Council.

## ■ REFERENCES


(1) Greene, M. Perylene Pigments. *High Perform. Pigment. Second Ed.* **2009**, *1*, 261−274.

(2) Herbst, W.; Hunger, K. *Industrial Organic Pigments*; Wiley-VCH, 2006; pp 1560−1560.

(3) Hains, A. W.; Liang, Z.; Woodhouse, M. A.; Gregg, B. A. Molecular Semiconductors in Organic Photovoltaic Cells. *Chem. Rev.* **2010**, *110* (11), 6689−6735.

(4) Feng, J.; Jiang, W.; Wang, Z. Synthesis and Application of Rylene Imide Dyes as Organic Semiconducting Materials. *Chem. - An Asian J.* **2018**, *13* (1), 20−30.

(5) Nowak-Król, A.; Shoyama, K.; Stolte, M.; Würthner, F. Naphthalene and Perylene Diimides-Better Alternatives to Fullerenes for Organic Electronics? *Chem. Commun.* **2018**, *54* (98), 13763−13772.

(6) Zong, L.; Zhang, H.; Li, Y.; Gong, Y.; Li, D.; Wang, J.; Wang, Z.; Xie, Y.; Han, M.; Peng, Q.; Li, X.; Dong, J.; Qian, J.; Li, Q.; Li, Z. Tunable Aggregation-Induced Emission Nanoparticles by Varying Isolation Groups in Perylene Diimide Derivatives and Application in Three-Photon Fluorescence Bioimaging. *ACS Nano* **2018**, *12* (9), 9532−9540.

(7) Zhao, Z.; Xu, N.; Wang, Y.; Ling, G.; Zhang, P. Perylene Diimide-Based Treatment and Diagnosis of Diseases. *J. Mater. Chem. B* **2021**, *9* (43), 8937−8950.

(8) Cheng, P.; Zhao, X.; Zhan, X. Perylene Diimide-Based Oligomers and Polymers for Organic Optoelectronics. *Accounts Mater. Res.* **2022**, *3* (3), 309−318.

(9) Krupka, O.; Hudhomme, P. Recent Advances in Applications of Fluorescent Perylenediimide and Perylenemonoimide Dyes in Bioimaging, Photothermal and Photodynamic Therapy. *Int. J. Mol. Sci.* **2023**, *24* (7), 6308.

(10) Akash; Tiwari, J. P. Recent Advancements in Perylene Diimide as an Electron Acceptor in Organic Solar Cells. *J. Mater. Chem. C* **2024**, *12* (3), 838−853.

(11) Sun, H.; Zhang, Q. Recent Advances in Perylene Diimides (PDI)-based Small Molecules Used for Emission and Photothermal Conversion. *ChemPhotoChem.* **2024**, *8* (3), No. e202300213.

(12) Nowak-Król, A.; Würthner, F. Progress in the Synthesis of Perylene Bisimide Dyes. *Org. Chem. Front.* **2019**, *6* (8), 1272−1318.

(13) Li, Y.; Zhang, X. L.; Liu, D. Recent Developments of Perylene Diimide (PDI) Supramolecular Photocatalysts: A Review. *J. Photochem. Photobiol. C Photochem. Rev.* **2021**, *48*, 100436.

(14) Hou, Y.; Zhang, Z.; Ma, L.; Shi, R.; Ling, S.; Li, X.; He, G.; Zhang, M. Perylene Diimide-Based Multicomponent Metallacages as Photosensitizers for Visible Light-Driven Photocatalytic Oxidation Reaction. *CCS Chem.* **2022**, *4* (8), 2604−2611.

(15) Li, H.; Wenger, O. S. Photophysics of Perylene Diimide Dianions and Their Application in Photoredox Catalysis. *Angew. Chemie - Int. Ed.* **2022**, *61* (5), 1−9.

(16) Shang, X.; Li, Z.; Jiao, J.; Fu, W.; Gao, K.; Peng, X.; Wang, Z.; Zhuo, H.; Yang, C.; Yang, M.; Chang, G.; Yang, L.; Zheng, X.; Yan, Y.; Chen, F.; Zhang, M.; Meng, Z. Integration of Perylene Diimide into a Covalent Organic Framework for Photocatalytic Oxidation. *Angew. Chemie Int. Ed.* **2024**, *63* (46), No. e202412977.

(17) Yang, B.; Lu, L.; Liu, S.; Cheng, W.; Liu, H.; Huang, C.; Meng, X.; Rodriguez, R. D.; Jia, X. Recent Progress in Perylene Diimide Supermolecule-Based Photocatalysts. *J. Mater. Chem. A* **2024**, *12* (7), 3807−3843.

(18) Wang, X.; Yang, A. Enhancing Oxygen Evolution: Novel Bay-Substituted Perylene Diimide Polymers with Phenol Groups as High-Performance Photocatalysts. *ACS Appl. Energy Mater.* **2024**, *7* (14), 5781−5791.

(19) Xu, H.; Xia, S.; Li, C.; Li, Y.; Xing, W.; Jiang, Y.; Chen, X. Programming Tetrathiafulvalene-Based Covalent Organic Frameworks for Promoted Photoinduced Molecular Oxygen Activation. *Angew. Chemie Int. Ed.* **2024**, *63* (29), No. e202405476.

(20) Nosaka, Y.; Nosaka, A. Y. Generation and Detection of Reactive Oxygen Species in Photocatalysis. *Chem. Rev.* **2017**, *117* (17), 11302−11336.

(21) Li, Q.; Li, F.-t. Recent Advances in Molecular Oxygen Activation via Photocatalysis and Its Application in Oxidation Reactions. *Chem. Eng. J.* **2021**, *421* (April), 129915.
(22) Agostinis, P.; Berg, K.; Cengel, K. A.; Foster, T. H.; Girotti, A. W.; Gollnick, S. O.; Hahn, S. M.; Hamblin, M. R.; Juzeniene, A.; Kessel, D.; Korbelik, M.; Moan, J.; Mroz, P.; Nowis, D.; Piette, J.; Wilson, B. C.; Golab, J. Photodynamic Therapy of Cancer: An Update. *CA. Cancer J. Clin.* **2011**, *61* (4), 250−281.
(23) Singh, N.; Sen Gupta, R.; Bose, S. A Comprehensive Review on Singlet Oxygen Generation in Nanomaterials and Conjugated Polymers for Photodynamic Therapy in the Treatment of Cancer. *Nanoscale* **2024**, *16* (7), 3243−3268.
(24) Zhang, J.; Ma, W.; Luo, H.; Zhang, K.; Lv, J.; Jiang, L.; Huang, Y.; Song, J.; Yang, Z.; Huang, W. Toward Type I/II ROS Generation Photoimmunotherapy by Molecular Engineering of Semiconducting Perylene Diimide. *Adv. Healthc. Mater.* **2024**, *13* (8), 1−10.
(25) Liu, C.; Ji, C.; Fan, Z.; Ma, R.; Yin, M. A Facile Design of Thio-Perylenediimides with Controllable Fluorescent, Photodynamic and Photothermal Effects towards Cancer Theranostics. *Chem. Commun.* **2021**, *57* (97), 13126−13129.
(26) Blacha-Grzechnik, A.; Drewniak, A.; Walczak, K. Z.; Szindler, M.; Ledwon, P. Efficient Generation of Singlet Oxygen by Perylene Diimide Photosensitizers Covalently Bound to Conjugate Polymers. *J. Photochem. Photobiol. A Chem.* **2020**, *388*, No. 112161.
(27) Kearns, D. R. Physical and Chemical Properties of Singlet Molecular Oxygen. *Chem. Rev.* **1971**, *71* (4), 395−427.
(28) Schweitzer, C.; Schmidt, R. Physical Mechanisms of Generation and Deactivation of Singlet Oxygen. *Chem. Rev.* **2003**, *103* (5), 1685−1757.
(29) Turro, N. J.; Scaiano, J. C.; Ramamurthy, V. *Principles of Molecular Photochemistry: An Introduction*; University Science Books: CA, 2009.
(30) Wardle, B. *Principles and Applications of Photochemistry*; Wiley-VCH: Weinheim, 2009.
(31) Huang, S.; Ye, C.; Chen, S.; Liang, Z.; Zhou, Y.; Wang, X. Highly-Efficient NIR Sensitization of Palladiumphthalocyanine with Peripheral $\sigma$-$\pi$ Conjugation Effect. *J. Lumin.* **2021**, *230*, No. 117709.
(32) Deng, F.; Sommer, J. R.; Myahkostupov, M.; Schanze, K. S.; Castellano, F. N. Near-IR Phosphorescent Metalloporphyrin as a Photochemical Upconversion Sensitizer. *Chem. Commun.* **2013**, *49* (67), 7406−7408.
(33) Felter, K. M.; Fravventura, M. C.; Koster, E.; Abellon, R. D.; Savenije, T. J.; Grozema, F. C. Solid-State Infrared Upconversion in Perylene Diimides Followed by Direct Electron Injection. *ACS Energy Lett.* **2020**, *5* (1), 124−129.
(34) Shibano, Y.; Umeyama, T.; Matano, Y.; Tkachenko, N. V.; Lemmetyinen, H.; Araki, Y.; Ito, O.; Imahori, H. Large Reorganization Energy of Pyrrolidine-Substituted Perylenediimide in Electron Transfer. *J. Phys. Chem. C* **2007**, *111* (16), 6133−6142.
(35) Campos, I. S.; Fermi, A.; Ventura, B.; Moraes, C. A. F.; Ribeiro, G. H.; Venâncio, T.; Ceroni, P.; Carlos, R. M. Modulation of the Excited States of Ruthenium(II)-Perylene Dyad to Access Near-IR Luminescence, Long-Lived Perylene Triplet State and Singlet Oxygen Photosensitization. *Inorg. Chem.* **2024**, *63* (10), 4595−4603.
(36) Sun, P.; Wang, X.; Wang, G.; Deng, W.; Shen, Q.; Jiang, R.; Wang, W.; Fan, Q.; Huang, W. A Perylene Diimide Zwitterionic Polymer for Photoacoustic Imaging Guided Photothermal/Photodynamic Synergistic Therapy with Single near-Infrared Irradiation. *J. Mater. Chem. B* **2018**, *6* (20), 3395−3403.
(37) Gryszel, M.; Schlossarek, T.; Würthner, F.; Natali, M.; Głowacki, E. D. Water-Soluble Cationic Perylene Diimide Dyes as Stable Photocatalysts for H 2 O 2 Evolution. *ChemPhotoChem.* **2023**, *7* (9), e202300070.
(38) Carloni, P.; Damiani, E.; Greci, L.; Stipa, P.; Tanfani, F.; Tartaglini, E.; Wozniak, M. On the Use of 1,3-Diphenylisobenzofuran (DPBF). Reactions with Carbon and Oxygen Centered Radicals in Model and Natural Systems. *Res. Chem. Intermed.* **1993**, *19* (5), 395−405.
(39) Ohyashiki, T.; Nunomura, M.; Katoh, T. Detection of Superoxide Anion Radical in Phospholipid Liposomal Membrane by Fluorescence Quenching Method Using 1,3-Diphenylisobenzofuran. *Biochim. Biophys. Acta - Biomembr.* **1999**, *1421* (1), 131−139.
(40) Demmig, S.; Langhals, H. Leichtlösliche, Lichtechte Perylen-Fluoreszenzfarbstoffe. *Chem. Ber.* **1988**, *121* (2), 225−230.
(41) Ramírez, M. G.; Pla, S.; Boj, P. G.; Villalvilla, J. M.; Quintana, J. A.; Díaz-García, M. A.; Fernández-Lázaro, F.; Sastre-Santos, Á. 1,7-Bay-Substituted Perylenediimide Derivative with Outstanding Laser Performance. *Adv. Opt. Mater.* **2013**, *1* (12), 933−938.
(42) Pérez-Ojeda, M. E.; Zink-Lorre, N.; Pla, S.; Zink, A.; Sastre-Santos, Á.; Fernández-Lázaro, F.; Hirsch, A. Influence of Substituents of Perylenebisimides on the Surface Energy and Wettability: A Systematic Structure−Property Relationship Analysis. *Dye. Pigment.* **2022**, *199*, 110044.
(43) Signoretto, M.; Zink-Lorre, N.; Suarez, I.; Font-Sanchis, E.; Sastre-Santos, Á.; Chirvony, V. S.; Fernández-Lázaro, F.; Martínez-Pastor, J. P. Efficient Optical Amplification in a Sandwich-Type Active-Passive Polymer Waveguide Containing Perylenediimides. *ACS Photonics* **2017**, *4* (1), 114−120.
(44) Muñoz-Mármol, R.; Zink-Lorre, N.; Villalvilla, J. M.; Boj, P. G.; Quintana, J. A.; Vázquez, C.; Anderson, A.; Gordon, M. J.; Sastre-Santos, Á.; Fernández-Lázaro, F.; Díaz-García, M. A. Influence of Blending Ratio and Polymer Matrix on the Lasing Properties of Perylenediimide Dyes. *J. Phys. Chem. C* **2018**, *122* (43), 24896−24906.
(45) Epelde-Elezcano, N.; Martínez-Martínez, V.; Peña-Cabrera, E.; Gómez-Durán, C. F. A.; Arbeloa, I. L.; Lacombe, S. Modulation of Singlet Oxygen Generation in Halogenated BODIPY Dyes by Substitution at Their: Meso Position: Towards a Solvent-Independent Standard in the Vis Region. *RSC Adv.* **2016**, *6* (48), 41991−41998.
(46) Solymosi, I.; Krishna, S.; Nuin, E.; Maid, H.; Scholz, B.; Guldi, D. M.; Pérez-Ojeda, M. E.; Hirsch, A. Diastereoselective Formation of Homochiral Flexible Perylene Bisimide Cyclophanes and Their Hybrids with Fullerenes. *Chem. Sci.* **2021**, *12* (47), 15491−15502.
(47) Van Stokkum, I. H. M.; Larsen, D. S.; Van Grondelle, R. Global and Target Analysis of Time-Resolved Spectra. *Biochim. Biophys. Acta - Bioenerg.* **2004**, *1657* (2−3), 82−104.
(48) Leeuw, P. M. J. d. An Introduction to the Special Volume on "Psychometrics in R". *J. Stat. Softw.* **2007**, *20* (1), 1−5.
(49) Snellenburg, J. J.; Laptenok, S. P.; Seger, R.; Mullen, K. M.; Stokkum, I. H. M. v. Glotaran: A Java-Based Graphical User Interface for the R Package TIMP. *J. Stat. Softw.* **2012**, *49* (3), 1−22.
(50) Bannwarth, C.; Ehlert, S.; Grimme, S. GFN2-XTB - An Accurate and Broadly Parametrized Self-Consistent Tight-Binding Quantum Chemical Method with Multipole Electrostatics and Density-Dependent Dispersion Contributions. *J. Chem. Theory Comput.* **2019**, *15* (3), 1652−1671.
(51) Neese, F. Software Update: The ORCA Program System—Version 5.0. *Wiley Interdiscip. Rev. Comput. Mol. Sci.* **2022**, *12* (5), 1−15.
(52) Frisch, M. J.; Trucks, G. W.; Schlegel, H. B.; Scuseria, G. E.; Robb, M. a.; Cheeseman, J. R.; Scalmani, G.; Barone, V.; Petersson, G. a.; Nakatsuji, H.; Li, X.; Caricato, M.; Marenich, a. V.; Bloino, J.; Janesko, B. G.; Gomperts, R.; Mennucci, B.; Hratchian, H. P.; Ortiz, J. V.; Izmaylov, a. F.; Sonnenberg, J. L.; Williams; Ding, F.; Lipparini, F.; Egidi, F.; Goings, J.; Peng, B.; Petrone, A.; Henderson, T.; Ranasinghe, D.; Zakrzewski, V. G.; Gao, J.; Rega, N.; Zheng, G.; Liang, W.; Hada, M.; Ehara, M.; Toyota, K.; Fukuda, R.; Hasegawa, J.; Ishida, M.; Nakajima, T.; Honda, Y.; Kitao, O.; Nakai, H.; Vreven, T.; Throssell, K.; Montgomery, Jr., J. a.; Peralta, J. E.; Ogliaro, F.; Bearpark, M. J.; Heyd, J. J.; Brothers, E. N.; Kudin, K. N.; Staroverov, V. N.; Keith, T. a.; Kobayashi, R.; Normand, J.; Raghavachari, K.; Rendell, a. P.; Burant, J. C.; Iyengar, S. S.; Tomasi, J.; Cossi, M.; Millam, J. M.; Klene, M.; Adamo, C.; Cammi, R.; Ochterski, J. W.; Martin, R. L.; Morokuma, K.; Farkas, O.; Foresman, J. B.; Fox, D. J. *Gaussian 16, Revision C.01*; Gaussian, Inc.: Wallingford, CT.
(53) Grimme, S.; Antony, J.; Ehrlich, S.; Krieg, H. A Consistent and Accurate Ab Initio Parametrization of Density Functional Dispersion

Correction (DFT-D) for the 94 Elements H-Pu. *J. Chem. Phys.* **2010**, *132* (15), 154104.
(54) Rablen, P. R.; Pearlman, S. A.; Finkbiner, J. A Comparison of Density Functional Methods for the Estimation of Proton Chemical Shifts with Chemical Accuracy. *J. Phys. Chem. A* **1999**, *103* (36), 7357−7363.
(55) Lecklider, T. Maintainng a Heathy Rhythm. *EE Eval. Eng.* **2011**, *50* (11), 36−39.
(56) Hanwell, M. D.; Curtis, D. E.; Lonie, D. C.; Vandermeersch, T.; Zurek, E.; Hutchison, G. R. Avogadro: An Advanced Semantic Chemical Editor, Visualization, and Analysis Platform. *J. Cheminform.* **2012**, *4* (1), 17.
(57) Lee, Y.; Jo, A.; Park, S. B. Rational Improvement of Molar Absorptivity Guided by Oscillator Strength: A Case Study with Furoindolizine-Based Core Skeleton. *Angew. Chemie - Int. Ed.* **2015**, *54* (52), 15689−15693.
(58) Tanaka, Y.; Tajima, K.; Kusumoto, R.; Kobori, Y.; Fukui, N.; Shinokubo, H. End-to-End Bent Perylene Bisimide Cyclophanes by Double Sulfur Extrusion. *J. Am. Chem. Soc.* **2024**, *146* (23), 16332−16339.
(59) Pagoaga, B.; Mongin, O.; Caselli, M.; Vanossi, D.; Momicchioli, F.; Blanchard-Desce, M.; Lemercier, G.; Hoffmann, N.; Ponterini, G. Optical and Photophysical Properties of Anisole-and Cyanobenzene-Substituted Perylene Diimides. *Phys. Chem. Chem. Phys.* **2016**, *18* (6), 4924−4941.
(60) Crovini, E.; Zhang, Z.; Kusakabe, Y.; Ren, Y.; Wada, Y.; Naqvi, B. A.; Sahay, P.; Matulaitis, T.; Diesing, S.; Samuel, I. D. W.; Brütting, W.; Suzuki, K.; Kaji, H.; Bräse, S.; Zysman-Colman, E. Effect of a Twin-Emitter Design Strategy on a Previously Reported Thermally Activated Delayed Fluorescence Organic Light-Emitting Diode. *Beilstein J. Org. Chem.* **2021**, *17*, 2894−2905.
(61) Ou, Q.; Peng, Q.; Shuai, Z. Toward Quantitative Prediction of Fluorescence Quantum Efficiency by Combining Direct Vibrational Conversion and Surface Crossing: BODIPYs as an Example. *J. Phys. Chem. Lett.* **2020**, *11* (18), 7790−7797.
(62) Xu, C.; Ye, R.; Shen, H.; Lam, J. W. Y.; Zhao, Z.; Zhong Tang, B. Molecular Motion and Nonradiative Decay: Towards Efficient Photothermal and Photoacoustic Systems. *Angew. Chemie - Int. Ed.* **2022**, *61* (30), No. e202204604.
(63) Snellenburg, J. J.; Laptenok, S. P.; Seger, R.; Mullen, K. M.; Stokkum, I. H. M. v. Glotaran : A Java -Based Graphical User Interface for the R Package TIMP. *J. Stat. Softw.* **2012**, *49* (3), 1−22.
(64) Mayländer, M.; Nolden, O.; Franz, M.; Chen, S.; Bancroft, L.; Qiu, Y.; Wasielewski, M. R.; Gilch, P.; Richert, S. Accessing the Triplet State of Perylenediimide by Radical-Enhanced Intersystem Crossing. *Chem. Sci.* **2022**, *13* (22), 6732−6743.
(65) Ford, W. E.; Kamat, P. V. Photochemistry of 3,4,9,10-Perylenetetracarboxylic Dianhydride Dyes. 3. Singlet and Triplet Excited-State Properties of the Bis(2,5-Di-Tert-Butylphenyl)Imide Derivative. *J. Phys. Chem.* **1987**, *91* (25), 6373−6380.
(66) Dubey, R. K.; Niemi, M.; Kaunisto, K.; Stranius, K.; Efimov, A.; Tkachenko, N. V.; Lemmetyinen, H. Excited-State Interaction of Red and Green Perylene Diimides with Luminescent Ru(II) Polypyridine Complex. *Inorg. Chem.* **2013**, *52* (17), 9761−9773.
(67) Wollscheid, N.; Pérez Lustres, J. L.; Kefer, O.; Hahn, S.; Brosius, V.; Bunz, U. H. F.; Motzkus, M.; Buckup, T. Oxygen-Catalysed Sequential Singlet Fission. *Nat. Commun.* **2019**, *10* (1), 1−7.
(68) Stuart, A. N.; Kee, T. W.; Huang, D. M. Role of Singlet and Triplet Excited States in the Oxygen-Mediated Photophysics and Photodegradation of Polyacenes. *J. Am. Chem. Soc.* **2024**, *146* (3), 2174−2186.
(69) Wilkinson, F.; McGarvey, D. J.; Olea, A. F. Factors Governing the Efficiency of Singlet Oxygen Production during Oxygen Quenching of Singlet and Triplet States of Anthracene Derivatives in Cyclohexane Solution. *J. Am. Chem. Soc.* **1993**, *115* (25), 12144−12151.


https://doi.org/10.1021/aps.5c00002
*Artif. Photosynth.* XXXX, XXX, XXX−XXX